nature physics

ARTICLES

PUBLISHED ONLINE: 21 JULY 2013 | DOI: 10.1038/NPHYS2685

Mapping the orbital wavefunction of the surface states in three-dimensional topological insulators

Yue Cao[1]*, J. A. Waugh[1], X-W. Zhang[2,3], J-W. Luo[3], Q. Wang[1†], T. J. Reber[1†], S. K. Mo[4], Z. Xu[5], A. Yang[5], J. Schneeloch[5], G. D. Gu[5], M. Brahlek[6], N. Bansal[6], S. Oh[6], A. Zunger[7] and D. S. Dessau[1]*

Understanding the structure of the wavefunction is essential for depicting the surface states of a topological insulator. Owing to the inherent strong spin–orbit coupling, the conventional hand-waving picture of the Dirac surface state with a single chiral spin texture is incomplete, as this ignores the orbital components of the Dirac wavefunction and their coupling to the spin textures. Here, by combining orbital-selective angle-resolved photoemission experiments and first-principles calculations, we deconvolve the in-plane and out-of-plane *p*-orbital components of the Dirac wavefunction. The in-plane orbital wavefunction is asymmetric relative to the Dirac point. It is predominantly tangential (radial) to the *k*-space constant energy surfaces above (below) the Dirac point. This orbital texture switch occurs exactly at the Dirac point, and therefore should be intrinsic to the topological physics. Our results imply that the Dirac wavefunction has a spin–orbital texture—a superposition of orbital wavefunctions coupled with the corresponding spin textures.

The topological surface state[1–3] provides a new avenue for realizing spintronic devices and quantum computation[4,5]. Both applications require manipulating the wavefunction to achieve select spin configurations; and thus most of the research so far has focused exclusively on the spin degree of freedom[6–11]. However, because strong spin–orbit coupling is inherent in all the known topological insulators (TIs), spin is not a good quantum number and does not provide a complete description of the Dirac state. Instead, the orbital portion of the total wavefunction to which spins are strongly coupled is also critical for describing the topological surface states. It is natural to expect that the spin texture has to be locked to the orbital wavefunction in a specific manner. Actually, it is proposed that the total angular momentum **J**, defined as the sum of electron spin **s** and orbital angular momentum **L**, may be a conserved quantity[8,12]. Studying the orbital degree of freedom as well as its coupling to the helical spin texture is thus indispensable both for understanding the topological physics and for future applications.

Although the existence of the Dirac state is determined by tracking the time reversal symmetry of the bulk bands[13–15], its effective description can be constructed by considering the time reversal and real space symmetries of the surface state itself, without information from the bulk bands. To investigate which features of the Dirac state the 'effective model' captures, we need to check both the spin and orbital properties of the electronic wavefunction. These questions motivate us to explore the orbital aspects of the Dirac states.

Within the prevailing description of the Dirac state[7,12,16,17], we expect (Supplementary Information) that the in-plane part of the orbital wavefunction in the vicinity of the Dirac point is symmetric relative to the Dirac point. As we will show, this is counter to our experimental observation here.

To investigate the orbital wavefunction on both sides of the Dirac point, we choose the prototypical three-dimensional TIs Bi_2Se_3 and Bi_2Te_3 as our main subjects of study. As shown in refs 16,17, the bulk and Dirac bands are all made of the out-of-plane p_z orbitals, because the in-plane p_x and p_y orbitals are well separated from the p_z orbitals by strong crystal field effects. However, for the Dirac surface states, the strong spin–orbit coupling explicitly mixes the in-plane states with the p_z orbitals. We will focus on the in-plane states here, as they show new and unexpected physics.

Angle-resolved photoemission spectroscopy (ARPES) provides a unique opportunity to directly measure k-state orbital structures with different symmetries, through the photon polarization selection rules[18] (often termed 'the matrix element effect'). The measured ARPES intensity $I \propto |\langle\psi_f|\mathbf{A}\cdot\mathbf{p}|\psi_i\rangle|^2 \propto |\langle\psi_f|\mathbf{E}\cdot\mathbf{r}|\psi_i\rangle|^2$ where $\mathbf{A}$ is the electromagnetic gauge and $\mathbf{p}$ is the electron momentum; $\mathbf{E}$ is the electric field vector and $|\langle\psi_f|\mathbf{E}\cdot\mathbf{r}|\psi_i\rangle|^2$ is the integration over the entire real space. $|\psi_i\rangle$ and $|\psi_f\rangle$ represent the initial state of the electron in the solid and the final state of the photoexcited electron, respectively. In the presence of a linearly polarized electric field, only electronic states $|\psi_i\rangle$ of a particular symmetry will contribute to the measured ARPES intensity. This is because the matrix element includes integration across all spatial dimensions, so if the parity of the product $\langle\psi_f|\mathbf{A}\cdot\mathbf{p}|\psi_i\rangle$ is overall odd with respect to a particular mirror plane, the integration goes to zero and the ARPES intensity vanishes. By properly arranging the experimental geometry, it is often possible to adjust the parity of $|\psi_f\rangle$ and $|\mathbf{A}\cdot\mathbf{p}|$ such that the ARPES intensity vanishes in a certain direction, thus determining the parity (symmetry) of the initial state wavefunction $|\psi_i\rangle$. Using these carefully designed orbital-selective ARPES experiments to determine the symmetry of the initial state orbitals is the goal of the present work.

As discussed above, to a very good approximation we only need to consider the p-like wavefunctions[7,16,17] for the Dirac states and bulk bands nearest to the Dirac point. In the experiment, the

[1]Department of Physics, University of Colorado, Boulder, Colorado 80309, USA, [2]Department of Physics, Colorado School of Mines, Golden, Colorado 80401, USA, [3]National Renewable Energy Laboratory, Golden, Colorado 80401, USA, [4]Advanced Light Source, Lawrence Berkeley National Lab, Berkeley, California 94720, USA, [5]Condensed Matter Physics and Materials Science Department, Brookhaven National Laboratory, Upton, New York 11973, USA, [6]Department of Physics and Astronomy, Rutgers University, Piscataway, New Jersey 08854, USA, [7]University of Colorado, Boulder, Colorado 80309, USA. †Present addresses: Los Alamos National Laboratory, Los Alamos, New Mexico 87545, USA (Q.W.); Condensed Matter Physics and Material Science Department, Brookhaven National Laboratory, Upton, New York 11973, USA (T.J.R.). *e-mail: ycao@colorado.edu; Dessau@colorado.edu

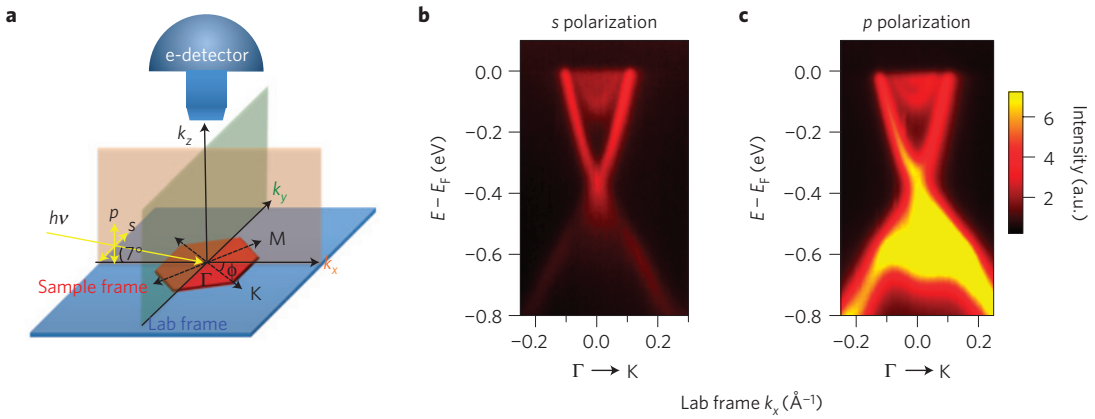

Figure 1 | ARPES energy–momentum intensity plots at the Γ point for *s* and *p* photon polarizations. a, The experimental configuration, where the sample frame is shown in red and the laboratory frame (which contains the electron detector) in blue. The sample axes can be rotated through the angle θ relative to the laboratory frame, though the normals of the sample and laboratory frames always stay aligned. The incident photon beam makes an angle of ∼7° relative to the laboratory (and sample) planes and has varying polarizations ranging from full *s* (**E** field parallel to the sample plane) to full *p* (**E** field in the orange k_x–k_z plane). **b**,**c**, ARPES cuts along the Γ–K direction of Bi_2Se_3 taken with *s* (**b**) and *p* (**c**) polarization, with the sample Γ–K axis lying in the k_x laboratory frame direction. Colour scale applies to **b**,**c**.

incident photons come at a glancing angle ∼7 ° to the sample plane and can have either *p* polarization (photon electric field vector, drawn with yellow arrow, in the orange-coloured scattering plane) or *s* polarization (**E** field perpendicular to the scattering plane). These possibilities are illustrated in Fig. 1a. In both configurations, only the electron analyser is rotated to collect data, so that the relative angles between the sample coordinate axes and the photon beam coordinates (polarization and Poynting or incident vector) remain unchanged. Detailed information about the ARPES setup and data taking can be found in Supplementary Information.

The **E** field of *p* polarization points almost exclusively out of plane. Therefore, it leads to a strong ARPES cross-section for the out-of-plane p_z orbitals and a weak cross-section for the in-plane orbitals. In contrast, *s*-polarization data have a strong cross-section for the in-plane orbitals and a weak cross-section for the out-of-plane orbitals. This is observed in the energy–momentum intensity plot along the Γ–K cut of Bi_2Se_3, taken with *s* and *p* polarization respectively (Fig. 1b,c). The ARPES intensity of the Dirac cone is ∼3 times stronger using *p* polarization than using *s* polarization, confirming that the Dirac states have a large p_z component and non-negligible contribution from in-plane states. In addition to the surface states that make up the Dirac cone, the bulk valence band can also be observed in the interior of the Dirac cone below the Dirac point using *p* polarization. This indicates that the bulk valence band has a major p_z component, consistent with refs 16,17.

Figure 2 a shows constant energy surfaces of Bi_2Se_3 for different energies relative to the Dirac point (left to right) and for both polarizations (*s* and *p* as marked on the right of the panel). The bottom row shows data from *p* polarization, mainly made up of the p_z states. These are seen to be almost uniform around the constant energy surfaces for all energy cuts. In contrast, the data taken with *s* polarization have drastic intensity changes around the constant energy surfaces. In particular, the data above the Dirac point (left two columns) both show vanishing spectral weight parallel to the electric field, whereas the data below the Dirac point (right two columns) show suppressed spectral weight normal to the electric field. To determine whether this weight distribution is related to a specific crystalline orientation (sample frame) or relative to the photon field (laboratory frame), we rotated the sample crystalline axes in multiple 5° steps of the angle ϕ (Fig. 1a) about the sample normal while keeping all other experimental parameters the same. These data, shown in Fig. 2b from left to right columns, are almost identical with sample rotation, illustrating that this pattern is not due to any particular arrangement relative to the sixfold crystalline axes but is more general.

We now use a symmetry analysis across various mirror planes to disentangle the symmetries of the various in-plane states that contribute, requiring us to only consider *s*-polarized photons. A helpful mirror plane to consider is the one defined by the sample surface normal and the photon Poynting vector (orange plane in Fig. 1a, in the k_x direction in the laboratory frame, and shown as the orange lines in Fig. 2c). Relative to this k_x–k_z laboratory-based mirror plane, the *s*-polarized photon field **E** has an odd parity, whereas it has an even parity relative to the green k_y–k_z mirror plane. The free-electron final state $|\psi_f\rangle$ is even with respect to both these mirror planes. As labelled in Fig. 2c, this constrains the initial state wavefunctions $|\psi_i\rangle$ to have a certain parity with respect to these mirror planes, so that the ARPES intensity will vanish in the correct symmetry locations if the overall parity of the matrix element is odd. Above the Dirac point, the in-plane states along the green Γ–k_y line, and thus the initial state $|\psi_i\rangle$, must have odd symmetry with respect to this mirror plane (Fig. 2c, top) for a zero matrix element. Similarly, for the in-plane states below the Dirac point, there is vanishing weight along the orange Γ–k_x line and so the initial state is even with respect to this mirror plane (Fig. 2c, bottom). Along k_x above the Dirac point and along k_y below the Dirac point, there is strong spectral weight, the matrix elements are overall even, and the initial state parities can similarly be determined. Note that neither of these mirror planes is necessarily along any of the high symmetry crystalline directions of the sample, as is seen from the data of Fig. 2b.

We could deduce from Fig. 2c the in-plane *p* orbitals $|\psi_i\rangle$ that are consistent with the symmetry constraints discussed above, that is, odd with respect to the orange and green mirror planes above the Dirac point and even with respect to these planes below the Dirac point. These orbital wavefunctions are tangential to the constant energy surface above the Dirac point and then switch to being radial to the constant energy surface below the Dirac point. This is shown more clearly in Fig. 3 as the orange orbitals, showing the out-of-plane p_z components of the wavefunction in green. It is quite evident from symmetry analysis that linear polarization cleanly disentangles ARPES intensity contributions from different *p* orbitals (see Supplementary Information for more details), whereas the circular polarization used in previous experiments[19–22] focused on the spin chirality or the 'handedness' of the wavefunctions.

The measured orbital texture is captured in our first-principles calculations on the basis of the local density approximation.

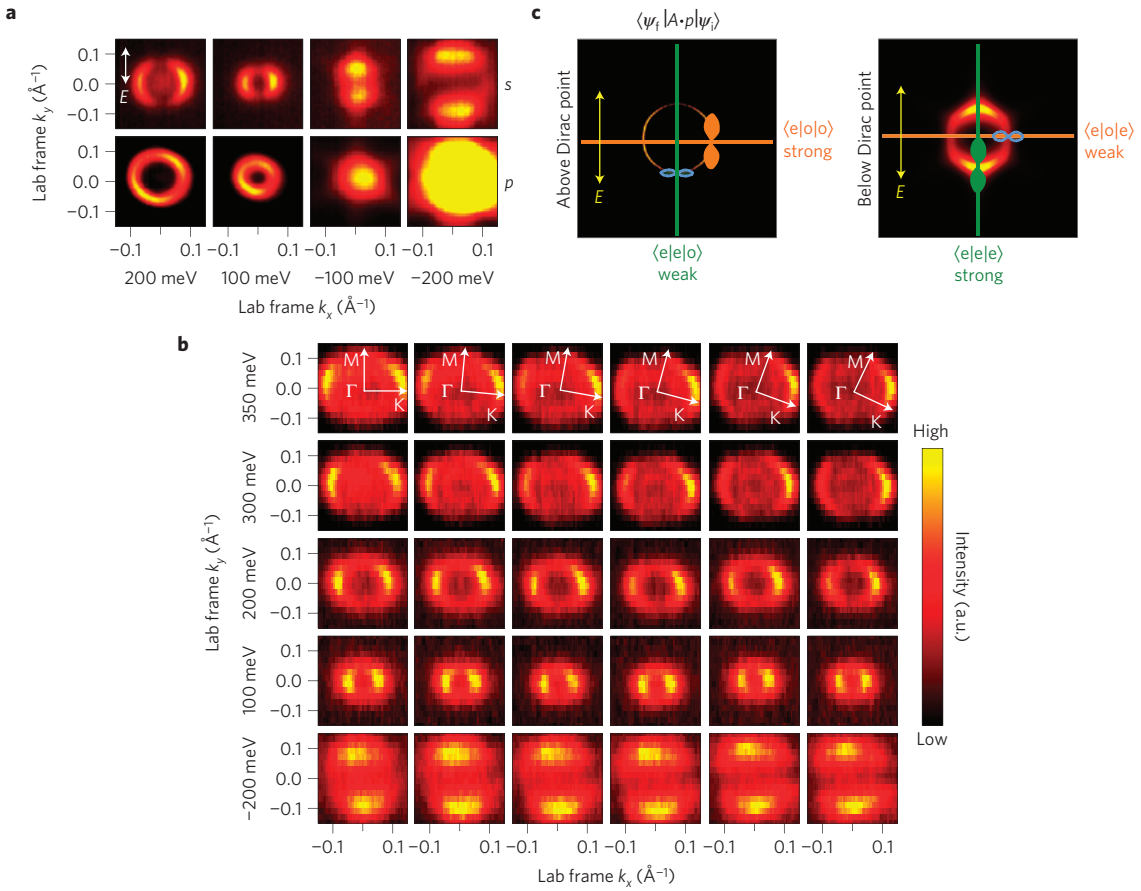

Figure 2 | Deducing the orbital texture from constant energy surface intensity plots. Data taken from Bi_2Se_3. **a**, The experimental constant energy surface intensity plot at different energies relative to the Dirac point. The Γ–K direction of Bi_2Se_3 is parallel to the laboratory k_x. **b**, *s*-polarization experimental constant energy surface intensity plots as a function of in-plane sample orientation and energies relative to the Dirac point, in 5° steps, from left to right columns. The axes shown are the crystal axes that are attached to the lattice orientation. The laboratory frame direction is unchanged as the sample is rotated, and all energy labels are relative to the Dirac point. **c**, Symmetry analysis of *p* orbitals across the orange k_x–k_z and green k_y–k_z laboratory-frame mirror planes (see also Fig. 1a). The free electron final state $|\psi_f\rangle$ is even in all cases, whereas the *s*-polarized photon field $|A\cdot p|$ is odd with respect to the orange k_x–k_z mirror plane and even with respect to the green k_y–k_z mirror plane. As illustrated, this gives strong or weak intensity for initial states $|\psi_i\rangle$ with symmetry that has the total matrix element even or odd, respectively. Because this result is independent of sample rotation (**b**), it implies an in-plane tangential orbital texture above the Dirac point and a radial one below (Fig. 3).

The calculated Dirac surface bands, the bulk conduction band and the bulk valence band nearest to the Dirac point of Bi_2Se_3 and Bi_2Te_3 are drawn in Fig. 4a,d. The experimental ARPES configuration carried out with *s*-polarized incident photons is replicated in the calculations by projecting the intensity of the p_y orbital (Supplementary Information). In Fig. 4b we show the calculated p_y orbital intensity of the Dirac state for Bi_2Se_3 on constant energy surfaces above and below the Dirac point, each summing over a 20 meV energy window. The calculation well reproduces the experimental measurement of the orbital texture of the Dirac state. For example, above the Dirac point, the calculated p_y component maximizes along the laboratory axis k_x and minimizes along k_y (where the p_x orbital dominates the in-plane states). Similar to the experiment, we also found that rotating the sample axes relative to the laboratory frame through angle ϕ has minimal effect on the calculated p_y intensity distribution, especially near the Dirac point. We discuss more details of the first-principles calculation in Methods and in the Supplementary Information.

To further trace the origin of the orbital texture switch of the Dirac state, we would like to zoom in close to the Dirac point, as this is the region where the Dirac physics is least affected by lattice effects or hybridization to the bulk bands. Due to the limit of experimental resolution we explore this near-Dirac point region using the calculated orbital densities. The calculated p_y orbital intensity for each constant energy surface is shown as a function of sample azimuth angle (as defined in Fig. 4b) in Fig. 4c. Most notable is the switch of the intensity distribution above and below the Dirac point, which is a signature of the orbital texture switch. Moreover, as the energy approaches the Dirac point, the intensity variation fits very well to a $\sin 2\theta$ or $\cos 2\theta$ distribution. At 300 meV above the Dirac point, the intensity curve shows a sixfold modulation on top of the $\cos 2\theta$ function. This further modulation might come from the hybridization to the bulk bands, or from the non-isotropic term of spin–orbit coupling[23]. To quantify this we define the orbital polarization ratio (OPR) λ as a function of either energy relative to the Dirac point ω or momentum ($|\mathbf{k}|$) relative to the Dirac point

$$\lambda(\omega) = \frac{I_0(\omega) - I_{90}(\omega)}{I_0(\omega) + I_{90}(\omega)} \quad \text{or} \quad \lambda(|\mathbf{k}|) = \frac{I_0(|\mathbf{k}|) - I_{90}(|\mathbf{k}|)}{I_0(|\mathbf{k}|) + I_{90}(|\mathbf{k}|)}$$

where I_θ is the calculated p_y orbital intensity around the constant energy surface, with the 0° angle in θ defined in Fig. 4b (note that this angle is relative to the laboratory frame, whereas the angle ϕ is between the sample and laboratory frame— Figs 1 and 2). $\lambda > (<)\ 0$ indicates there is a larger proportion of the tangential

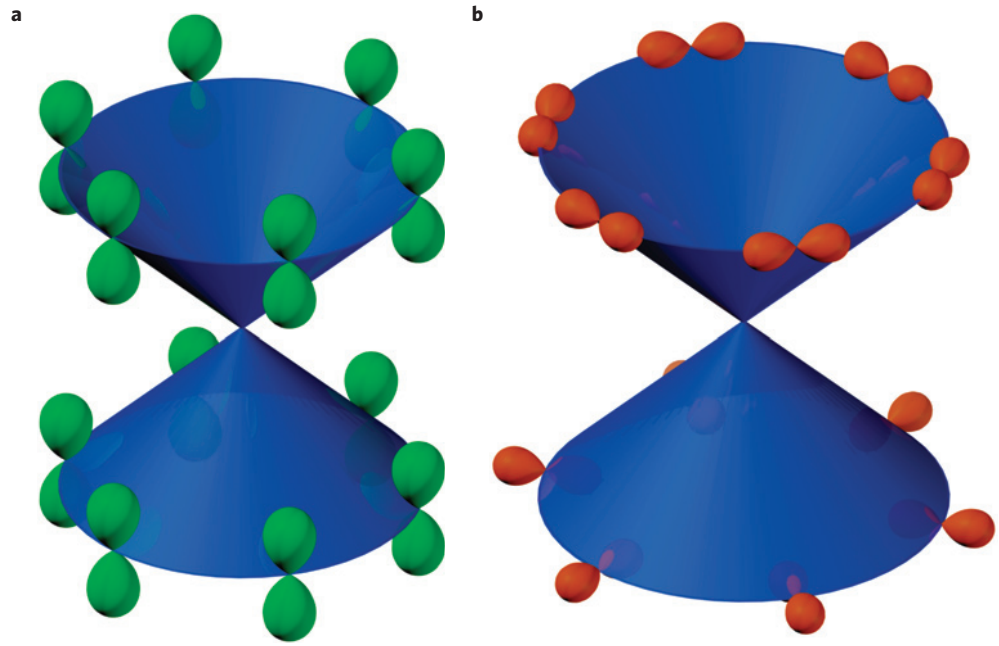

Figure 3 | Sketch of the orbital texture switch deduced from the experimental and theoretical matrix elements. a, The green orbitals are of p_z character and are viewed with *p*-polarized light. **b**, The red orbitals represent the in-plane p_x/p_y components of the orbital wavefunction and are summed so that the net in-plane wavefunctions are polarized to be more tangential to the constant energy surface above the Dirac point and more radial below the Dirac point.

(radial) in-plane orbital. Figure 4e,f show that this switch occurs exactly at the Dirac point for both Bi_2Se_3 and Bi_2Te_3.

Analysis of the λ-dependence on electron momentum and energy yields the wavefunction of the topological state in the vicinity of the Dirac point

$$|\psi(k)\rangle_+ = \sqrt{(1-\alpha)}|p_z\rangle \otimes |\mathrm{LHS}\rangle + \sqrt{\frac{\alpha}{2}}[(1+\beta|k|)|p_\mathrm{t}\rangle \otimes |s_\mathrm{t}\rangle + (1-\beta|k|)|p_\mathrm{r}\rangle \otimes |s_\mathrm{r}\rangle]$$

and

$$|\psi(k)\rangle_- = \sqrt{(1-\alpha)}|p_z\rangle \otimes |\mathrm{RHS}\rangle + \sqrt{\frac{\alpha}{2}}[(1-\beta|k|)|p_\mathrm{t}\rangle \otimes |s_\mathrm{t}\rangle + (1+\beta|k|)|p_\mathrm{r}\rangle \otimes |s_\mathrm{r}]$$

where $\pm$ denotes the wavefunction above/below the Dirac point, α and β are (complex) coefficients and $|p_{z,\mathrm{t,r}}\rangle$ stands for the p_z, tangential and radial in-plane p orbitals, respectively. $|\mathrm{LHS/RHS}\rangle$ are initial state left-handed and right-handed spin textures consistent with all previous spin-resolved measurements and calculations, and $\otimes$ is the cross-product between the orbital and spin degrees of freedom. We leave the spin texture of the in-plane components for future explorations (note added and also refs 24,25) and mark them as $|s_{\mathrm{t,r}}\rangle$. The proposed wavefunction has the following characteristics.

First, the coefficient $\alpha \sim 1/2$ is the fraction of the p orbitals with in-plane character, as determined from our first-principles calculation (Supplementary Information), with a slight variation of α as a function of momentum. Both experiment and calculation show that the in-plane orbital components account for a significant part of the Dirac wavefunction.

Second, the terms with $\beta|k|$ reflect how fast the in-plane orbitals become predominantly tangential, $|p_\mathrm{t}\rangle$, or radial, $|p_\mathrm{r}\rangle$, away from the Dirac point. At the Dirac point ($k = 0$) the terms with $\beta|k|$ disappear and the Dirac wavefunction has an equal proportion of radial and tangential in-plane orbitals. These statements come from the fact that λ linearly approaches zero as the energy (Fig. 4e) or momentum (Fig. 4f) approaches the Dirac point and, to within the statistical error, changes sign exactly at the Dirac point.

Third, the orbital content of the wavefunction can be approximately determined by using only two parameters, α and β. Although we might have expected different β coefficients above and below the Dirac point, the fact that the slopes of λ versus k are almost equal above and below the Dirac point ($\sim$13 Å for Bi_2Se_3 and 11 Å for Bi_2Te_3, deduced from the slope of the curves in Fig. 4f) suggests that we need only a single β coefficient. As discussed in subsequent works[24,25], the spin components of the wavefunction are locked to the orbital component, so these two parameters tell us about the spin as well.

The form of a spin–orbital coupled Dirac wavefunction as discussed above invites future orbital-selective spin-resolved measurements of $|s_{\mathrm{t,r}}\rangle$, and thus we could determine the full Dirac wavefunction. This provides a vital clue to whether the total angular momentum J is conserved.

Our observation that the orbital texture switches exactly at the Dirac point in two TIs with quite distinct electronic structures provides strong evidence that the orbital polarization switch is an intrinsic feature of the Dirac surface state. The Dirac point of Bi_2Te_3 is much closer ($<$20 meV) to the bulk valence band than Bi_2Se_3, and the surface state dispersion bends upward below the Dirac point, in stark contrast to Bi_2Se_3, which has the more 'ideal' Dirac-like linear dispersion. Despite the significant differences in the surface state dispersions, the two compounds show an almost identical behaviour of the OPR λ, which changes sign exactly at the Dirac point in both cases. This new behaviour indicates the unexpected richness of the surface states of TIs. Although the underlying symmetries that are responsible for this generic switching behaviour have not yet been unearthed, complete effective models of the topological state should apparently include these features.

Note added in proof: Following the initial submission of this paper, a follow-up theoretical work[24] confirmed the in-plane orbital texture switch that was first shown here. Further, the authors of ref. 24 show a coupled spin–orbital texture of the topological surface state by analytically solving the general spin–orbit coupling Hamiltonian,

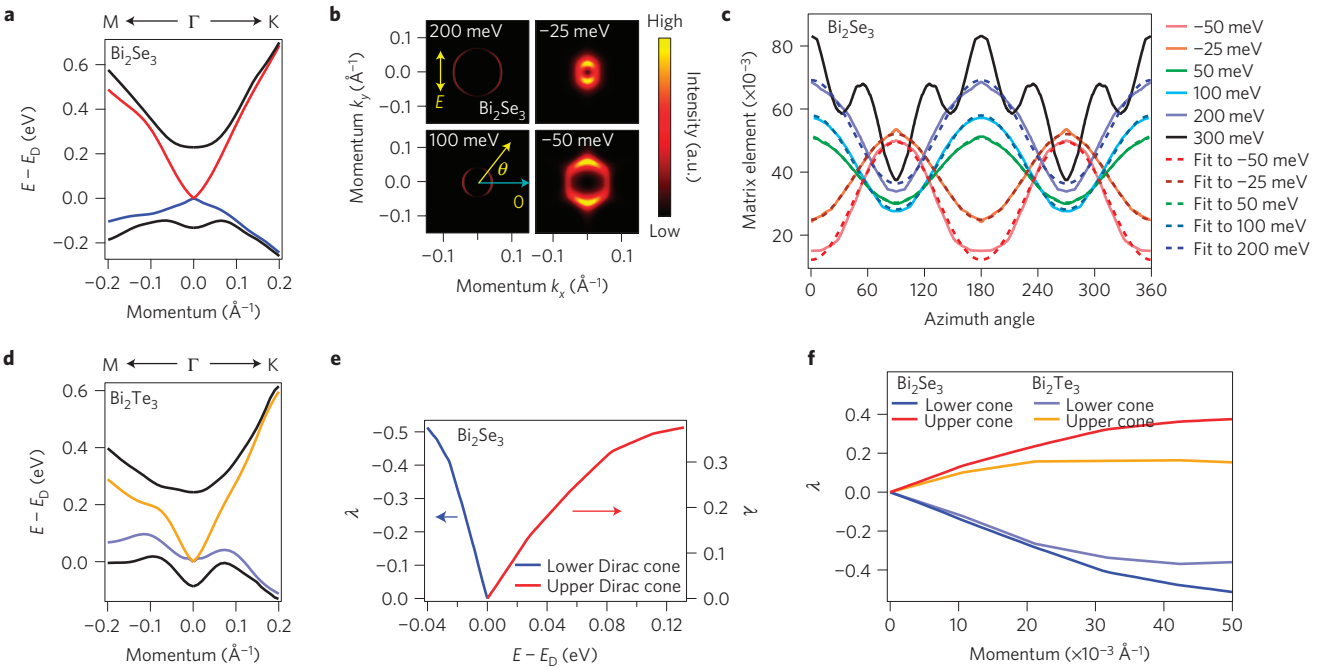

Figure 4 | OPR λ switches sign at the Dirac point. a,**d**, First-principles calculation of Bi_2Se_3 and Bi_2Te_3, only showing the Dirac bands (upper/lower Dirac cones in red/blue and yellow/purple solid lines for **a** and **d** respectively) and the bulk bands closest to the Dirac point. **b**, Calculated p_y orbital intensity at different energies relative to the Dirac point of Bi_2Se_3, each summed over a window of 20 meV relative to the central energy shown on the plot. **c**, For each energy relative to the Dirac point of Bi_2Se_3, the calculated projected p_y orbital intensity as a function of the sample in-plane azimuth angle (for the definition of the azimuth angle, see **b**, with 0° as marked). The dashed lines are the selected $\cos 2\theta / \sin 2\theta$ fits to the calculated p_y intensities shown with solid lines. **e**, Calculated OPR λ of Bi_2Se_3 as a function of the energy relative to the Dirac point, and **f**, calculated λ of Bi_2Se_3 and Bi_2Te_3 as a function of momentum k. Note λ switches sign exactly at the Dirac point.

predicting that the in-plane tangential orbitals above the Dirac point couple with a right-handed spin texture, which is opposite to the well-known left-handed spin texture to which the out-of-plane orbitals couple. This prediction was directly confirmed by our orbital-selective and spin-resolved ARPES experiments[25], conclusively demonstrating the critical role of the orbital texture for the physics of the topological insulators.

Methods

The ARPES experiments were carried out at Beamline 10.0.1 of the Advanced Light Source, LBL. Data have been taken both from Bi_2Se_3 thin films and bulk samples and have shown consistent results. The Bi_2Se_3 thin films were prepared using a two-step growth method, as described in ref. 26 and Supplementary Information, and were protected with a Se overlayer after growth, and decapped *in situ* by heating in the final vacuum environment of the analysis chamber. The bulk samples were cleaved *in situ* at 50 K with a base pressure better than 5×10^{-11} torr.

We carried out calculations for six quintuple-layer slabs of Bi_2Se_3 and Bi_2Te_3. The orbital character of electronic states is obtained by projecting the calculated plane-wave-based wavefunctions $|\psi_{nk}\rangle$ onto spherical harmonics $|J_l^{R_i} Y_{lm}^{R_i}\rangle$ including p orbitals ($l = 1$) centred at the positions of the ions R_i.

$$|\psi_{nk}\rangle = \sum_{i}^{N_{at}} \sum_{lm} \alpha_{m,nk}^{R_i} |J_l^{R_i} Y_{lm}^{R_i}\rangle$$

where N_{at} is the total number of atomic sites. Also we choose an s-like ($l = 0$) final state to represent the electron state photon-excited to vacuum, so that it is always even with respect to the proposed mirror planes. The projection strategy is so chosen to bring about the symmetry information in the atomic orbitals, without contributions from any special mirror plane. We find that the Dirac cone states, especially those away from the Dirac point, are a hybridization of topological surface states and bulk states as shown by their wavefunction distribution. This feature of the topological states was found in two-dimensional HgTe/CdTe TI by some of us[27]. To distinguish the pure topological surface states from bulk band states, we projected the states layer by layer and summed up the contribution of each atomic orbital with an exponential weighting away from the surface, and we confirmed that the choice of decay distance does not affect the calculation qualitatively. The results shown in Fig. 4b have a decay distance of 0.5 nm, which approximates the ARPES probe depth.

Received 10 October 2012; accepted 6 June 2013; published online 21 July 2013

References

1. Qi, X. L. & Zhang, S. C. The quantum spin Hall effect and topological insulators. *Phys. Today* **63,** 33–38 (January, 2010).
2. Hasan, M. Z. & Kane, C. L. Colloquium: Topological insulators. *Rev. Mod. Phys.* **82,** 3045–3067 (2010).
3. Qi, X-L. & Zhang, S-C. Topological insulators and superconductors. *Rev. Mod. Phys.* **83,** 1057–1110 (2011).
4. Read, N. Topological phases and quasiparticle braiding. *Phys. Today* **65,** 38–43 (July, 2012).
5. Moore, J. E. The birth of topological insulators. *Nature* **464,** 194–198 (2010).
6. Basak, S. *et al.* Spin texture on the warped Dirac-cone surface states in topological insulators. *Phys. Rev. B* **84,** 121401(R) (2011).
7. Zhang, W., Yu, R., Zhang, H., Dai, X. & Fang, Z. First-principles studies of the three-dimensional strong topological insulators Bi_2Te_3, Bi_2Se_3 and Sb_2Te_3. *New J. Phys.* **12,** 065013 (2010).
8. Yazyev, O. V., Moore, J. E. & Louie, S. G. Spin polarization and transport of surface states in the topological insulators Bi_2Se_3 and Bi_2Te_3 from first principles. *Phys. Rev. Lett.* **105,** 266806 (2010).
9. Hsieh, D. *et al.* A tunable topological insulator in the spin helical Dirac transport regime. *Nature* **460,** 1101–1105 (2009).
10. Pan, Z-H. *et al.* Electronic structure of the topological insulator Bi_2Se_3 using angle-resolved photoemission spectroscopy: Evidence for a nearly full surface spin polarization. *Phys. Rev. Lett.* **106,** 257004 (2011).
11. Xia, Y. *et al.* Observation of a large-gap topological-insulator class with a single Dirac cone on the surface. *Nature Phys.* **5,** 398–402 (2009).
12. Park, S. R., Kim, C. H., Yu, J., Han, J. H. & Kim, C. Orbital-angular-momentum based origin of Rashba-type surface band splitting. *Phys. Rev. Lett.* **107,** 156803 (2011).
13. Fu, L., Kane, C. L. & Mele, E. J. Topological insulators in three dimensions. *Phys. Rev. Lett.* **98,** 106803 (2007).
14. Fu, L. & Kane, C. L. Topological insulators with inversion symmetry. *Phys. Rev. B* **76,** 045302 (2007).

15. Moore, J. E. & Balents, L. Topological invariants of time-reversal-invariant band structures. *Phys. Rev. B* **75,** 121306 (R) (2007).
16. Zhang, H. *et al.* Topological insulators in Bi_2Se_3, Bi_2Te_3 and Sb_2Te_3 with a single Dirac cone on the surface. *Nature Phys.* **5,** 438–442 (2009).
17. Liu, C-X. *et al.* Model Hamiltonian for topological insulators. *Phys. Rev. B* **82,** 045122 (2010).
18. Damascelli, A., Hussain, Z. & Shen, Z-X. Angle-resolved photoemission studies of the cuprate superconductors. *Rev. Mod. Phys.* **75,** 473–541 (2003).
19. Wang, Y. H. *et al.* Observation of a warped helical spin texture in Bi_2Se_3 from circular dichroism angle-resolved photoemission spectroscopy. *Phys. Rev. Lett.* **107,** 207602 (2011).
20. Ishida, Y. *et al.* Common origin of the circular-dichroism pattern in angle-resolved photoemission spectroscopy of $SrTiO_3$ and $Cu_xBi_2Se_3$. *Phys. Rev. Lett.* **107,** 077601 (2011).
21. Park, S. R. *et al.* Chiral orbital-angular momentum in the surface states of Bi_2Se_3. *Phys. Rev. Lett.* **108,** 046805 (2012).
22. Bian, G. *et al.* Illuminating the surface spin texture of the Giant-Rashba quantum-well system Bi/Ag(111) by circularly polarized photoemission. *Phys. Rev. Lett.* **108,** 186403 (2012).
23. Liang, F. Hexagonal warping effects in the surface states of the topological insulator Bi_2Te_3. *Phys. Rev. Lett.* **103,** 266801 (2009).
24. Zhang, H-J., Liu, C-X. & Zhang, S-C. Spin-orbital texture in topological insulators. Preprint at http://arxiv.org/abs/1211.0762 (2012).
25. Cao, Y. *et al.* Coupled spin-orbital texture in a prototypical topological insulator. Preprint at http://arxiv.org/abs/1211.5998 (2012).
26. Bansal, N. *et al.* Epitaxial growth of topological insulator Bi_2Se_3 film on Si(111) with atomically sharp interface. *Thin Solid Films* **520,** 224–229 (2011).
27. Luo, J-W. & Zunger, A. Design principles and coupling mechanisms in the 2D quantum well topological insulator HgTe/CdTe. *Phys. Rev. Lett.* **105,** 176805 (2010).

Acknowledgements

We acknowledge helpful discussions with S-C. Zhang, S-R. Park, M. Hermele, A. Essin and G. Chen. The ARPES work was carried out at the Advanced Light Source, LBL, and was supported by the DOE Office of Basic Science by grant DE-FG02-03ER46066 and by the NSF under DMR-1007014. A.Z., X-W.Z. and J-W.L. were supported as part of the Center for Inverse Design, an Energy Frontier Research Center funded by the US Department of Energy, Office of Science, Office of Basic Energy Sciences, under award number DEAC 36-08GO28308. X-W.Z. also acknowledges the administrative support of REMRSEC under NSF grant number DMR-0820518, Colorado School of Mines, Golden, Colorado. The Rutgers work was supported by IAMDN of Rutgers University, National Science Foundation (NSF DMR-0845464) and Office of Naval Research (ONR N000140910749), and the Brookhaven work was supported by the DOE under contract number DE-AC03-76SF00098. Both LBL and BNL are supported by the DOE, Office of Basic Energy Sciences.

Author contributions

Y.C. led the experimental data taking and analysis. J.A.W., Q.W. and T.J.R. helped with the data taking, and S.K.M. with the instrument and decapping procedure. X-W.Z., J-W.L. and A.Z. carried out the density functional calculations. Y.C., X-W.Z., J-W.L. and A.Z. analyzed the results from the first-principles calculations. Z.X., A.Y., J.S. and G.D.G. prepared the single crystal samples, and M.B., N.B. and S.O. prepared the thin film samples. Y.C. and D.S.D. did the majority of the paper writing (with contributions from all coauthors) and D.S.D. directed the overall project.

Additional information

Supplementary information is available in the online version of the paper. Reprints and permissions information is available online at www.nature.com/reprints. Correspondence and requests for materials should be addressed to Y.C. or D.S.D.

Competing financial interests

The authors declare no competing financial interests.